KSME

Springer

Journal of Mechanical Science and Technology 34 (7) 2020

Original Article
DOI 10.1007/s12206-020-0639-9

Keywords:
· Circular cylinder
· Natural convection
· Power law fluid
· Square enclosure

Correspondence to:
Man Yeong Ha
myha@pusan.ac.kr

Citation:
Pandey, S., Park, Y. G., Ha, M. Y. (2020). Flow and heat transfer characteristics of non-Newtonian fluid in a square enclosure containing an internal cylinder. Journal of Mechanical Science and Technology 34 (7) (2020) 3079~3094.
http://doi.org/10.1007/s12206-020-0639-9

Received January 23rd, 2020
Revised April 13th, 2020
Accepted May 4th, 2020

† Recommended by Editor
Yong Tae Kang

Flow and heat transfer characteristics of non-Newtonian fluid in a square enclosure containing an internal cylinder

Sudhanshu Pandey[1], Yong Gap Park[2] and Man Yeong Ha[1]

[1]School of Mechanical Engineering, Pusan National University, 2, Busandaehak-ro 63beon-gil, Geumjeong-gu, Busan 46241, Korea, [2]School of Mechanical Engineering, Changwon National University, 20, Changwondaehak-ro, Uichang-gu, Changwon 51140, Korea

Abstract Buoyancy-driven flows were investigated inside an enclosure with an inner cylinder embedded within it. The square enclosure contains the power law fluids. The effects are reported for the position of the cylinder along the horizontal and diagonal directions on the flow and thermal characteristics based on a rigorous unsteady numerical analysis. The cylinder was placed at several locations along the diagonal near the top-left corner, the center, and near the bottom right corner. The cylinder was also placed along the horizontal centerline near the right wall. This paper reports the effects of shear thickening and thinning fluids on the heat transfer mechanism in the enclosure. The thermal characteristics were more pronounced when the cylinder was near the bottom right corner than when near the top left corner and at the center. Pseudoplastic and dilatant fluids can be used in applications requiring increased and decreased heat transfer rates, respectively.

1. Introduction

Many researchers have studied the phenomenon of buoyancy-driven flows in enclosures of various shapes with internal bodies. The applications of natural convection can be found in the passive cooling of electronic components, air conditioning and solar energy. The investigation of laminar natural convection in the presence of power law fluids is needed for enhanced heat transfer characteristics. One of the reasons is the distinct performance of non-Newtonian fluids, such as dilatant and pseudoplastic fluids.

Ostrach [1] characterized the researches on free convection inside horizontal and rectangular cylinders and annuli subjected to discrete boundary conditions. Davis [2] summarized the benchmark solutions of 2D free convection for $10^3 \le Ra \le 10^6$. The flow and thermal performance is enhanced when the internal bodies are subjected to Isothermal rather than Iso heat flux boundary conditions [3].

Kim et al. [4] found symmetric flow conditions about the center vertical line for $10^3 \le Ra \le 10^6$. Hussain and Hussein [5] analyzed the same physical domain as that of Kim et al. [4] with an internal cylinder but with constant heat-flux as a boundary condition. Unsteady flow arises at a higher Rayleigh number depending on the position of the internal body [6]. Lee et al. [7] reported slanted thermal plumes on top of an inner circular cylinder.

Kang et al. [8] extended the work of Lee et al. [7] to $Ra = 10^7$ and reported unsteadiness arising in the square enclosure. The heat transfer increases at all the boundaries except the lower wall with increasing Rayleigh number in the range of Rayleigh numbers of 10^3-10^6 [9]. Park et al. [10] reported enhanced thermal characteristics in a cold square cavity consisting two circular cylinders in comparison to an enclosure containing only one cylinder. The position of the local peaks of Nusselt numbers around the cylinder are governed by the gap between the enclosure walls and cylinders [11].

The Nusselt numbers were higher at the horizontal walls of an enclosure in case of two heated inner cylinders than when a square enclosure has one hot and cold cylinder each [12].

The asymmetric flows arise about the vertical center line at *Ra* of 10^5 and 10^6 in the case of multi inner cylinders [13]. Seo et al. [14, 15] reported the change from steady to unsteady flow regimes depending on the positions of inner cylinders. Pandey et al. [16] summarized the studies on free convection in enclosures with or without internal bodies.

Acrivos [17] reported the asymptotic solutions in the case of power law fluids. Ozoe and Churchill [18] discussed an algorithm developed to analyze natural convection for only Ellis and power law models. The Nusselt number increases with decreasing value of the power law index [19]. Ohta et al. [20] observed a rather complicated flow field due to a viscosity change when the fluid is pseudoplastic in nature at a high Rayleigh number in a square cavity using the Sutterby model. Kim et al. [21] delineated the influence of the power law index on the transient buoyant convection.

The heat transfer in the case of a tall rectangular cavity is mainly governed by the power law index and Rayleigh number at higher Prandtl numbers ($Pr > 100$), as reported by Lamsaadi et al. [22, 23]. The effect of the inclined rectangular cavity is more pronounced with decreasing power law index [24].

Turan et al. [25-27] developed a criterion that can predict the change of flow from steady to unsteady flow inside an enclosure. Matin and Khan [28] found that the Nusselt number increases by 170 % in the case of pseudoplastic fluids inside an annulus when compared with the case of Newtonian fluid. The flow transition takes place at $n = 0.6$ in the pseudoplastic regime, as proclaimed by Pandey et al. [29].

Unlike the case of Newtonian fluid, non-Newtonian power law fluids exhibits different natures such as pseudoplastic or dilatant based on the shear rate and temperature dependency. The novelty of present study stems from the fact that the flow and heat transfer characteristics of non-Newtonian fluids in these regimes are not well established yet and should be investigated thoroughly. Furthermore, many studies in past have been performed based on the steady state analysis. However, Pandey et al. [29] have reported an unsteadiness arising at higher Rayleigh number of 10^6 in the shear thinning regime ($n = 0.6$). The effects of an inner cylinder placed along the diagonal as well as horizontal centerlines on the behavior of non-Newtonian fluid have not been investigated so far. Hence, this paper focuses on analyzing the effects of the movement of an inner heated circular cylinder on laminar natural convection in an enclosure filled with non-Newtonian fluids. The cylinder was moved along the diagonal and horizontal center lines. The unsteadiness and asymmetry resulting from the position of inner cylinder are also reported.

In process of designing the thermal systems such as heat exchangers, electronic chip cooling system, the internal bodies such as circular cylinder must be placed at the optimized positions depending on the system requirement. The present study layout the optimized locations such as closed to the bottom wall for heat enhancement and center for the diminished heat transfer characteristics.

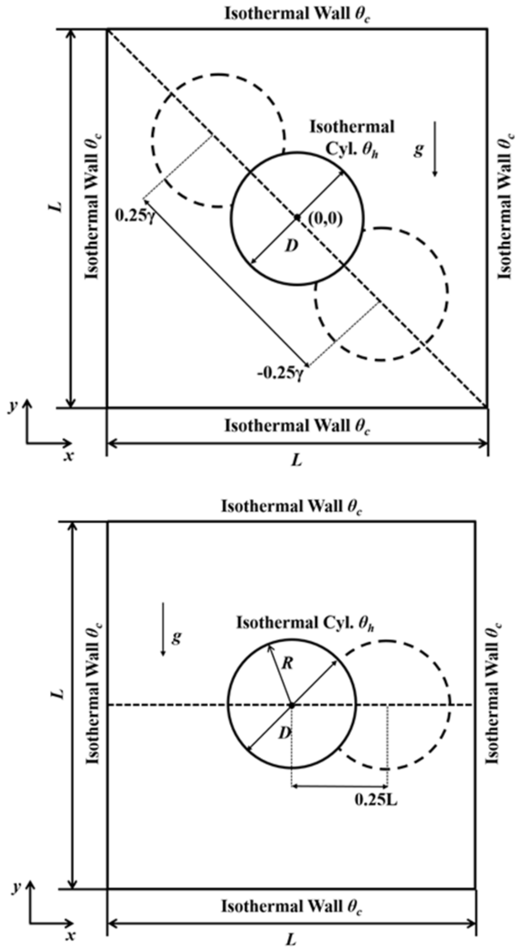

Fig. 1. Schematic diagram.

2. Numerical methodology

The physical system comprises a square enclosure subjected to cold temperature (θ_c) with length L, as shown in Fig. 1. A circular cylinder of radius *R* subjected to hot temperature (θ_h) is placed inside the enclosure. The cylinder was located at $\xi = 0.25\gamma$ (near the top left corner), $\xi = 0$ (center), and $\xi = -0.25\gamma$ (near the bottom right corner) along the diagonal line, where $\gamma = \sqrt{2}L$, as illustrated in Fig. 1. The cylinder was also positioned at $\delta = 0.25L$ along the horizontal center line, as shown in Fig. 1. The physical properties of non-Newtonian fluid are assumed to be constant except for the density that appears in the body force term of the Y-momentum equation.

The unsteady continuity, momentum and energy equations for incompressible laminar flow are defined as:

$$\frac{\partial U}{\partial X}+\frac{\partial V}{\partial Y}=0 \tag{1}$$

$$\frac{1}{Pr}\left(\frac{\partial U}{\partial \tau}+U\frac{\partial U}{\partial X}+V\frac{\partial U}{\partial Y}\right)=-\frac{\partial P}{\partial X}+2\frac{\partial H}{\partial X}\frac{\partial U}{\partial X}+\frac{\partial H}{\partial Y}\left(\frac{\partial U}{\partial Y}+\frac{\partial V}{\partial X}\right)+H\left(\frac{\partial^2 U}{\partial X^2}+\frac{\partial^2 U}{\partial Y^2}\right) \tag{2}$$

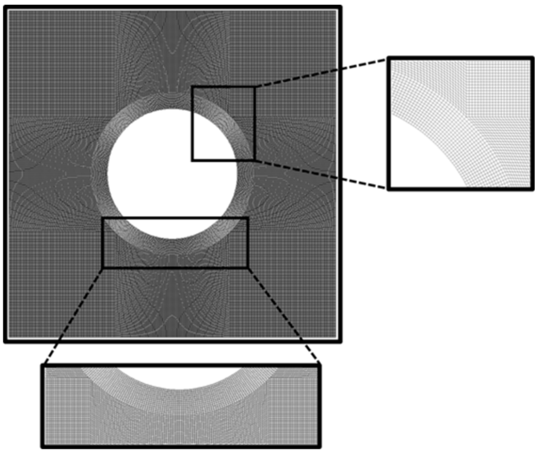

Fig. 2. Computational grid.

$$\frac{1}{Pr}\left(\frac{\partial V}{\partial \tau}+U\frac{\partial V}{\partial X}+V\frac{\partial V}{\partial Y}\right)=-\frac{\partial P}{\partial Y}+2\frac{\partial H}{\partial Y}\frac{\partial V}{\partial Y}+\frac{\partial H}{\partial X}\left(\frac{\partial U}{\partial Y}+\frac{\partial V}{\partial X}\right)+H\left(\frac{\partial^2 V}{\partial X^2}+\frac{\partial^2 V}{\partial Y^2}\right)+Ra\theta \quad (3)$$

$$\frac{\partial \theta}{\partial \tau}+U\frac{\partial \theta}{\partial X}+V\frac{\partial \theta}{\partial Y}=\frac{\partial^2 \theta}{\partial X^2}+\frac{\partial^2 \theta}{\partial Y^2}. \quad (4)$$

The effective viscosity (H) is defined as:

$$H=\frac{\eta}{m}=\left[2\left(\frac{\partial U}{\partial X}\right)^2+2\left(\frac{\partial V}{\partial Y}\right)^2+\left(\frac{\partial U}{\partial Y}+\frac{\partial V}{\partial X}\right)^2\right]^{\frac{n-1}{2}} \quad (5)$$

$$Pr=\frac{mL^{2-2n}}{\rho\alpha^{2-n}},\quad Ra=\frac{g\beta\Delta TL^{2n+1}}{\alpha^n\frac{m}{\rho}} \quad (6)$$

$$Nu=\left.\frac{\partial\theta}{\partial n_s}\right|_{wall},\quad \overline{Nu}=\frac{1}{W}\int_0^W Nu.dS \quad (7)$$

$$\langle Nu\rangle=\frac{1}{t_p}\int_{t_1}^{t_2}Nu.dt,\quad \langle\overline{Nu}\rangle=\frac{1}{t_p}\int_{t_1}^{t_2}\overline{Nu}\,dt \quad (8)$$

where n_s and W are the normal direction with respect to the walls and the surface area of the walls, respectively. t_p is the time period of integration.

The inner cylinder and enclosure were subjected to θ = 1 and θ = 0, respectively with no-slip conditions at the wall boundaries. All governing equations were solved using the finite-volume-based “Fluent” solver with SIMPLE scheme [30] used for pressure velocity coupling along with the Presto solver for solving the pressure equation.

It is important to mention at this juncture that the numerical methodology followed in the present study is similar to our previous studies [29]. Hence, the results of grid independence study as well as the validation studies are available elsewhere [29].

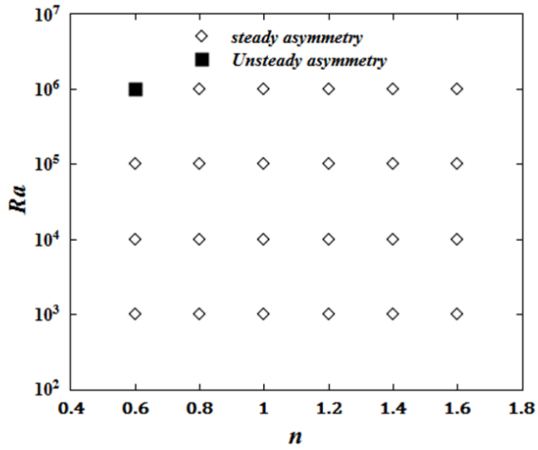

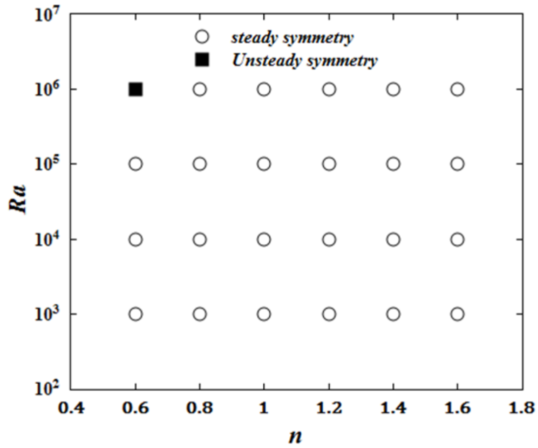

Fig. 3. Bifurcation maps for (a) ξ = -0.25γ, 0.25γ and δ = 0.25L; (b) ξ = 0.

3. Results and discussion

Bifurcation maps of the flow changing from steady to unsteady flow are shown in Fig. 3. The flow becomes unsteady at a power law index of 0.6 and higher Rayleigh number of 10^6. However, it ultimately reaches steady state for all the other cases considered. In addition, the symmetry in the flow and thermal fields that occurs in all cases at ξ = 0, as reported by Pandey et al. [29], disappears when the cylinder is positioned at ξ = 0.25γ, ξ = -0.25γ, and δ = 0.25L. The unsteadiness arising in the enclosure based on this CFD analysis also justifies the criteria given by Turan et al. [25] for the non-existence of two-dimensional steady solution, which state that it is impossible to obtain a 2D steady solution if:

$$Ra\geq\left[10^7.\mathrm{Pr}^{\frac{3n+1}{2n+2}}\right]^{\frac{2n+2}{5-n}} \quad (9)$$

$$Ra_{eff}\geq 10^8,\quad Ra_{eff}\approx Ra^{\frac{5-n}{2n+2}}.\mathrm{Pr}^{\frac{1-n}{2n+2}}. \quad (10)$$

The term on the right side of Eq. (9) was found to be 5.34×10^5, which corresponds to Pr = 10 and n = 0.6 and is less than $Ra = 10^6$. The effective Rayleigh number (Ra_{eff}) defined in Eq. (10) was found to be 2.37×10^8, which is higher than 10^8 corresponding to Pr = 10, $Ra = 10^6$, and n = 0.6. Therefore, both conditions violate the possible existence of a two-dimensional steady solution.

3.1 Flow and thermal fields

The CFD analysis was done for $10^3 \le Ra \le 10^6$ and $0.6 \le n \le 1.6$ in a step size of 0.2. The Isotherms and streamlines were obtained for n = 0.6, 1, and 1.6 for all Ra, ξ, and δ. The time-averaged isotherms and streamlines at n = 0.6, 1, and 1.6 for $10^3 \le Ra \le 10^6$ and $\xi = -0.25\gamma$ are shown in Fig. 4. The Isotherms and streamlines were asymmetric for all cases of $\xi = -0.25\gamma$. The isotherms were intensified at the bottom right corner near the cylinder, whereas coarsened isotherms were observed on the opposite corner of the enclosure, as depicted in Fig. 4. A weak thermal plume formed at n = 0.6 and $Ra = 10^3$, as revealed in Fig. 4(a). However, slanted thermal plumes appear at n = 0.6 and 1.0 at $Ra = 10^4$, as obvious in Figs. 4(d) and (e).

At n = 0.6, a heated plume reaches the upper boundary of the enclosure and scatters towards the vertical sidewalls, as manifested in Fig. 4(d). The streamlines show that a small inner vortex is generated in the lower right quarter. Moreover, the two inner vortices appearing inside the primary eddy in the left halve of the enclosure in case of n = 0.6, 1.0 and 1.6 for $Ra = 10^3$ and n = 1.0 and 1.6 for $Ra = 10^4$ when the cylinder is positioned at the center, as reported by Pandey et al. [29], merged into a large eddy in the respective cases of $\xi = -0.25\gamma$, as can be seen in Figs. 4(a)-(f).

The Isotherms and streamlines corresponding to $Ra = 10^5$ and 10^6 are shown in Figs. 4(g)-(l). The isotherms at $Ra = 10^5$ and 10^6 show larger ascending plumes in comparison to 10^3 and 10^4 due to increased buoyancy-driven flows. A thermal plume reaches the upper boundary of the enclosure in all cases at $Ra = 10^5$ and 10^6 due to higher velocity circulations in those regions with heated fluid. Figs. 4(g)-(l) exemplified that the stratification of isotherms takes place above the cylinder. Consequently, stronger thermal gradients occur at the location of the rising thermal plume.

The stratification is more dominant in the upper left quarter, as appears in Figs. 4(g) and (h). With increasing Rayleigh number to 10^6, the isotherms start to distort with stronger buoyancy. The thermal gradient near the boundary walls was also larger due to closely packed isotherms forming across the boundaries of cavity.

Analogous to the cases of $Ra = 10^3$ & 10^4, a small inner vortex appeared in the enclosure at n = 1.0 and 1.6 at $Ra = 10^5$ and 10^6. The flow circulation was identical in the left half of the enclosure at n = 1.6 for $Ra = 10^5$ & 10^6. However, with decreasing n, pseudoplastic effects start to overshadow dilatant effects, and the size of the right primary eddy increases, as shown in Fig. 4(k). The primary eddies in the left halve at n = 0.6 and $Ra = 10^5$ were composed of three inner vortices due to increasing shear thinning effects, as shown in Fig. 4(g). In addition, secondary vortices appeared around the cylinder and all corners of the enclosure.

Flow becomes unsteady corresponding to n = 0.6 and 10^6, and the isotherms become more intense across the enclosure walls, as shown in Fig. 4(j). The three inner vortices in the left primary eddy at n = 0.6 and $Ra = 10^5$ merged into one vortex with distorted flow at n = 0.6 and $Ra = 10^6$. Furthermore, reminiscent of n = 0.6 and $Ra = 10^5$, the streamlines show additional secondary vortices at different locations for n = 0.6 and $Ra = 10^6$ due to bifurcation of the flow. The flow appeared to be more confined in the right primary eddy for $Ra = 10^5$ & 10^6 with decreasing n of 0.6, as evident in Figs. 4(g) and (j).

Time-averaged thermal and flow domains at n = 0.6, 1, and 1.6 for $10^3 \le Ra \le 10^6$ and $\xi = 0.25\gamma$ are shown in Fig. 5. The Isotherms and streamlines were asymmetric for all cases of $\xi = 0.25\gamma$, similar to the case of $\xi = -0.25\gamma$. The isotherms were intensified at the top left corner near the cylinder, whereas coarsened isotherms were observed on the opposite corner of the cavity, revealed in Fig. 5. As demonstrated in Figs. 5(a)-(c), in case of $Ra = 10^3$, the isotherms exhibit a similar profile irrespective of the power law index due to the conduction-dominated flow regime.

As Ra increases to 10^4, isotherms start to bend towards the right vertical side walls with decreasing n. Isotherms corresponding to n = 0.6 depicts a weak heated plume, as indicated in Fig. 5(d). At n = 0.6, the heated plume reaches the right vertical walls, unlike the case of $Ra = 10^3$. As shown in Figs. 5(e) and (f), the heated fluid fails to reach to the right wall for n = 1.0 and 1.6 due to shear thickening effects. The streamlines show that a small inner vortex formed in between the cylinder and the top left corner.

The Isotherms and streamlines corresponding to $Ra = 10^5$ & 10^6 are shown in Figs. 5(g)-(l). The isotherms at $Ra = 10^5$ & 10^6 show larger slanted plumes than at 10^3 and 10^4 due to stronger buoyancy-driven flows. The thermal plume reaches the right vertical wall of the enclosure in all cases at $Ra = 10^5$ and 10^6 due to higher velocity circulations in the right halve. The temperature distributions at n = 1.0 and n = 1.6 at $Ra = 10^5$ were similar to those at n = 0.6 and n = 1.0 at $Ra = 10^4$, respectively, as shown in Figs. 5(h) and (i). However, two thermal plumes were formed at n = 0.6, as appeared in Fig. 5(g).

The flow circulation was identical in the case of n = 1.6 for $Ra = 10^5$ and 10^6, as shown in Figs. 5(i) and (l). The flow fields at n = 0.6 at $Ra = 10^5$ were somewhat different from other cases of n. The left primary eddy that was confined in the left half of the enclosure reaches the right half of the enclosure with more disturbed flow, as shown in Fig. 5(g). The stratification and distortion of isotherms take place above the cylinder as the Ra increases to 10^6, as highlighted in Figs. 5(k) and (l). Fig. 5(j) reveals that the stratification is more dominant near the right vertical wall. Accordingly, stronger thermal gradients occur near the right vertical wall.

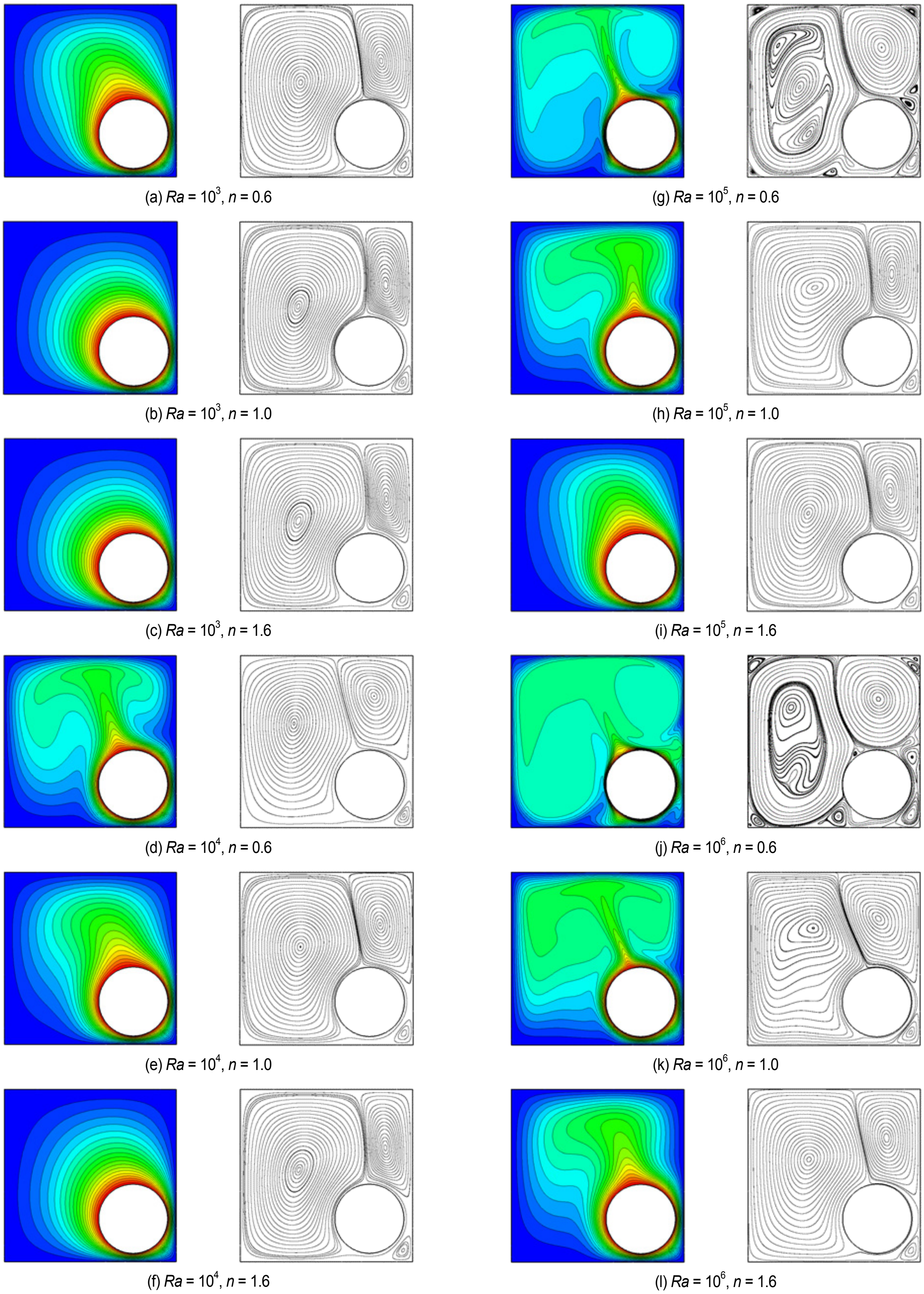

(a) $Ra = 10^3$, $n = 0.6$

(g) $Ra = 10^5$, $n = 0.6$

(b) $Ra = 10^3$, $n = 1.0$

(h) $Ra = 10^5$, $n = 1.0$

(c) $Ra = 10^3$, $n = 1.6$

(i) $Ra = 10^5$, $n = 1.6$

(d) $Ra = 10^4$, $n = 0.6$

(j) $Ra = 10^6$, $n = 0.6$

(e) $Ra = 10^4$, $n = 1.0$

(k) $Ra = 10^6$, $n = 1.0$

(f) $Ra = 10^4$, $n = 1.6$

(l) $Ra = 10^6$, $n = 1.6$

Fig. 4. Time-averaged isotherms and streamlines at $Pr = 10$ and $n = 0.6$, 1.0 and 1.6 for $\xi = -0.25y$ for various Ra.

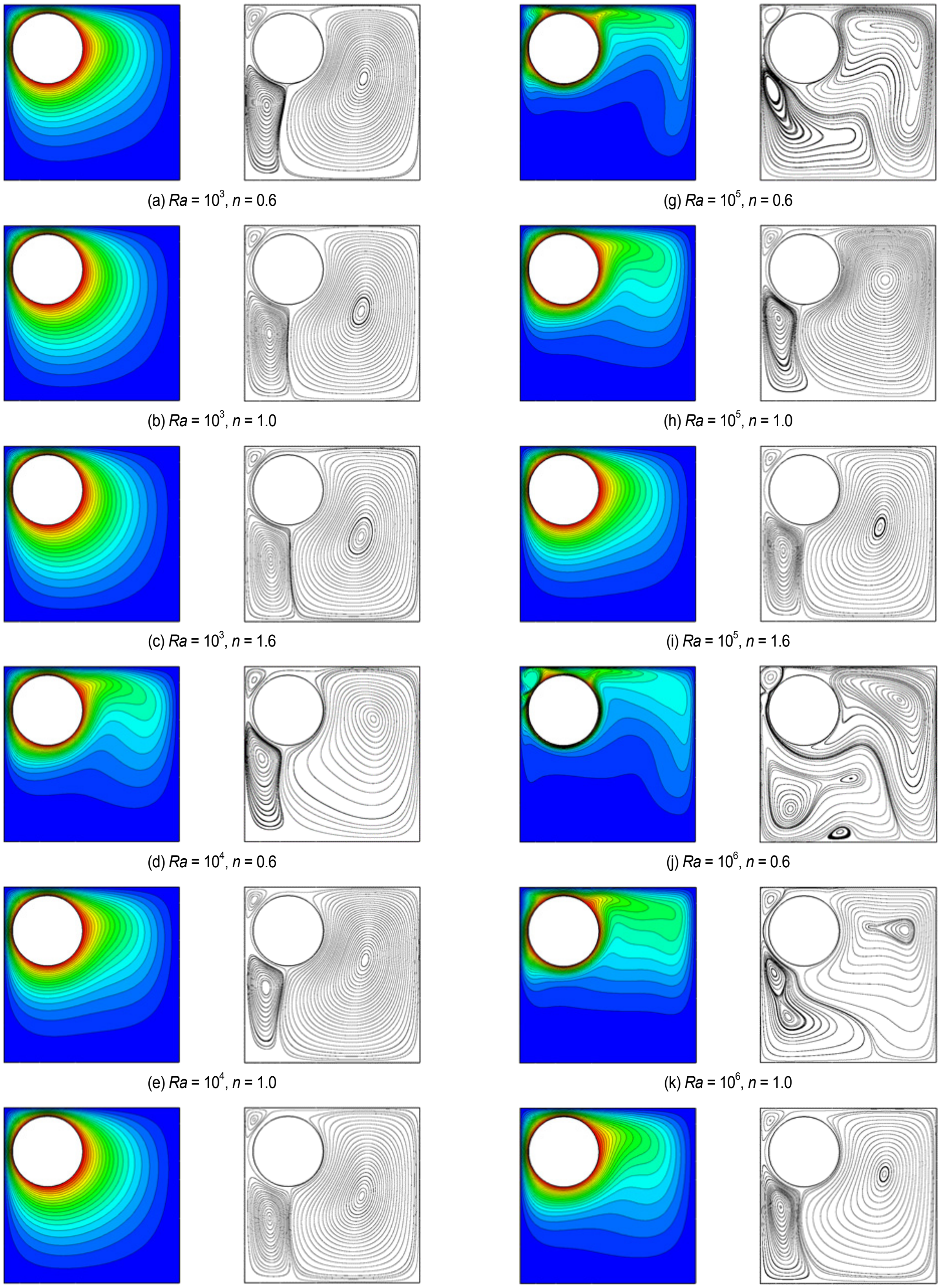
(a) $Ra = 10^3$, $n = 0.6$
(b) $Ra = 10^3$, $n = 1.0$
(c) $Ra = 10^3$, $n = 1.6$
(d) $Ra = 10^4$, $n = 0.6$
(e) $Ra = 10^4$, $n = 1.0$
(f) $Ra = 10^4$, $n = 1.6$
(g) $Ra = 10^5$, $n = 0.6$
(h) $Ra = 10^5$, $n = 1.0$
(i) $Ra = 10^5$, $n = 1.6$
(j) $Ra = 10^6$, $n = 0.6$
(k) $Ra = 10^6$, $n = 1.0$
(l) $Ra = 10^6$, $n = 1.6$

Fig. 5. Time-averaged isotherms and streamlines at $Pr = 10$ and $n = 0.6$, 1.0 and 1.6 for $\xi = 0.25y$ for various Ra.

There is a thinner thermal boundary layer across the cylinder for *Ra* = 10^6 at *n* = 0.6 due to increased convection and shear thinning effects. The left primary eddy with a single inner vortex splits into two inner vortices as *Ra* increases to 10^6 at *n* = 0.6 and 1.0 in comparison to the respective cases for *Ra* = 10^5, which can be seen in Figs. 5(j) and (k).

Moreover, a secondary vortex appears in the vicinity of lower wall. Flow found to be unsteady for *n* = 0.6 and 10^6, and the isotherms become more intense across the enclosure walls, as can be observed in Fig. 5(j).

The isotherms and streamlines at *n* = 0.6, 1, and 1.6 for $10^3 \le Ra \le 10^6$ and δ = 0.25L are illustrated in Fig. 6. The Isotherms and streamlines were symmetric about the horizontal center line at *Ra* = 10^3 for *n* = 1.0 and 1.6 and at *Ra* = 10^4 for *n* = 1.6, as shown in Figs. 6(b), (c) and (f). However, this symmetry breaks down at *n* = 0.6 for *Ra* = 10^3 and *n* = 0.6 and 1.0 for *Ra* = 10^4 due to shear thinning effects and the combined effects of increased buoyancy and shear thinning, respectively. The streamlines at *Ra* = 10^3 and *Ra* = 10^4 show one primary eddy in the left halve and two primary eddies in the right halve of the enclosure for all cases of *n*. However, the eye of the left primary eddy in the left half slightly moves in the upper half of the enclosure at *n* = 0.6 for *Ra* = 10^3 and *n* = 0.6 and 1.0 for *Ra* = 10^4, as shown in Figs. 6(a), (d) and (e). In addition, a plume rises above the cylinder corresponding to *Ra* = 10^4 and *n* = 0.6, as manifested in Fig. 6(d).

The flow and thermal domains were asymmetric about the horizontal center line of the enclosure at *Ra* of 10^5 and 10^6 for all cases due to stronger buoyancy flows, as shown in Figs. 6(g)-(l). The temperature and velocity distributions at *n* = 1.6 at *Ra* = 10^5 were identical to those of *n* = 1.0 and *Ra* = 10^4, as observed in Fig. 6(i). The thermal fields at *n* = 0.6 and 1.0 reach the upper wall because of the rising thermal plume above the cylinder, as shown in Figs. 6(g) and (h). At *n* = 1.0 and 1.6 for *Ra* = 10^5, the primary eddy in the left halve with one inner vortex bifurcates into three inner vortices at *n* = 0.6, as shown in Fig. 6(g). Furthermore, the primary eddy in the lower right halve with one vortex bifurcates into two inner vortices.

For *Ra* = 10^6, the isotherms distort, resulting in stratification along the vertical side walls. Figs. 6(j) and (k) revealed that the primary eddy in left halve with one inner vortex for *n* = 1.6 and *Ra* = 10^6 bifurcates into three and two inner vortices for *n* = 0.6 and *n* = 1.0, respectively. A transitional flow from steady to unsteady state at *n* = 0.6 and 10^6 is observed, and the isotherms become more intense across the enclosure walls, as shown in Fig. 6(j).

3.2 Unsteady dynamics

The evolution of $\overline{Nu}$ at inner cylinder over time is shown in Figs. 7(a)-(d) for ξ = -0.25γ, ξ = 0, ξ = 0.25*γ*, and δ = 0.25L corresponding to *Ra* = 10^6 and *n* = 0.6. The solution shows aperiodic unsteady oscillations. There is non-periodic sway of the thermal plume in either half of the enclosure, which causes the thickness of the thermal boundary to amend. Consequently, the distribution of the surface-averaged Nusselt number oscillates with time. Thereby, exhibiting asymmetric natures demonstrated in Figs. 4(j), 5(j) and 6(j) at *n* = 0.6 and *Ra* = 10^6.

The primary frequency distributions of the instantaneous surface-averaged Nusselt number around the cylinder for all cases are shown in Figs. 7(e) and (f). The primary frequencies for the cases of diagonal movements (ξ = -0.25γ, ξ = 0, and ξ = 0.25*γ*) are illustrated in Fig. 7(e). The oscillatory motion of the thermal plume rising on top of the cylinder is very strong in the case of ξ = -0.25γ. Consequently, the temperature and velocity distributions rapidly alter with time because of the strong sway of the thermal plume. For this reason, the highest dominant primary frequency is 402 Hz corresponding to *Ra* = 10^6 and *n* = 0.6.

However, for ξ = 0.25*γ*, the fluctuations are less intensified compared to the case of ξ = -0.25*γ*. Thus, lower primary frequency of 114 Hz. The lowest primary frequency among all cases is about 10 Hz in the case of ξ = 0 due to symmetrical thermal characteristics.

Similarly, the primary frequency for the cases of horizontal centerline movements (δ = -0.25L, δ = *0* or ξ = 0 and δ = 0.25L) are illustrated in Fig. 7(f). The results of only one case of horizontal movements are reported because the thermal and flow characteristics should be identical for δ = -0.25L and δ = 0.25L due to symmetrical positions along the horizontal centerline.

The primary frequency lies between those that occur at ξ = -0.25*γ* and ξ = 0.25*γ*. The space between the cylinder and top wall of the enclosure is larger than in the case of ξ = 0.25*γ*. This leads to stronger sway of the thermal plume on either side of the upper surface of the cylinder, and the additional plume rising on the right upper side of the cylinder appears and disappears over time. Therefore, the primary frequency of 210 Hz is higher than in the case of ξ = 0.25*γ*.

3.3 Distribution of local Nusselt number

The variation of $\langle Nu \rangle$ around the cylinder can be justified upon analyzing the thermal fields of respective cases. For the case of ξ = -0.25*γ*, the variations of $\langle Nu \rangle$ at *n* = 0.6 to 1.6 are shown in Fig. 8. The distribution of $\langle Nu \rangle$ at *Ra* = 10^3 shows two peak values at φ = 90° and 180°, irrespective of *n*, as manifested in Fig. 8(a). This is due to the highly packed isotherms in these regions, as shown in Figs. 4(a)-(c). Moreover, the variation of $\langle Nu \rangle$ at *n* = 0.6 is somewhat different from other cases in the range of $220^\circ \le \varphi \le 360^\circ$ due to slanted isotherms developing above the cylinder.

The distribution of $\langle Nu \rangle$ at *Ra* = 10^4 is similar to that at *Ra* = 10^3, especially at higher *n*, as shown in Fig. 8(b). However, with decreasing *n*, the variation of $\langle Nu \rangle$ with reference to φ shows a somewhat different increasing and decreasing trends except in the range of $70^\circ \le \varphi \le 210^\circ$. This is due to the slightly higher buoyancy-induced flow than that at *Ra* = 10^3, as shown in Fig. 8(b). The distribution of $\langle Nu \rangle$ at *Ra* = 10^5 is similar to that at *Ra* = 10^4 except at *n* = 0.6, as shown in Fig. 8(c). Two

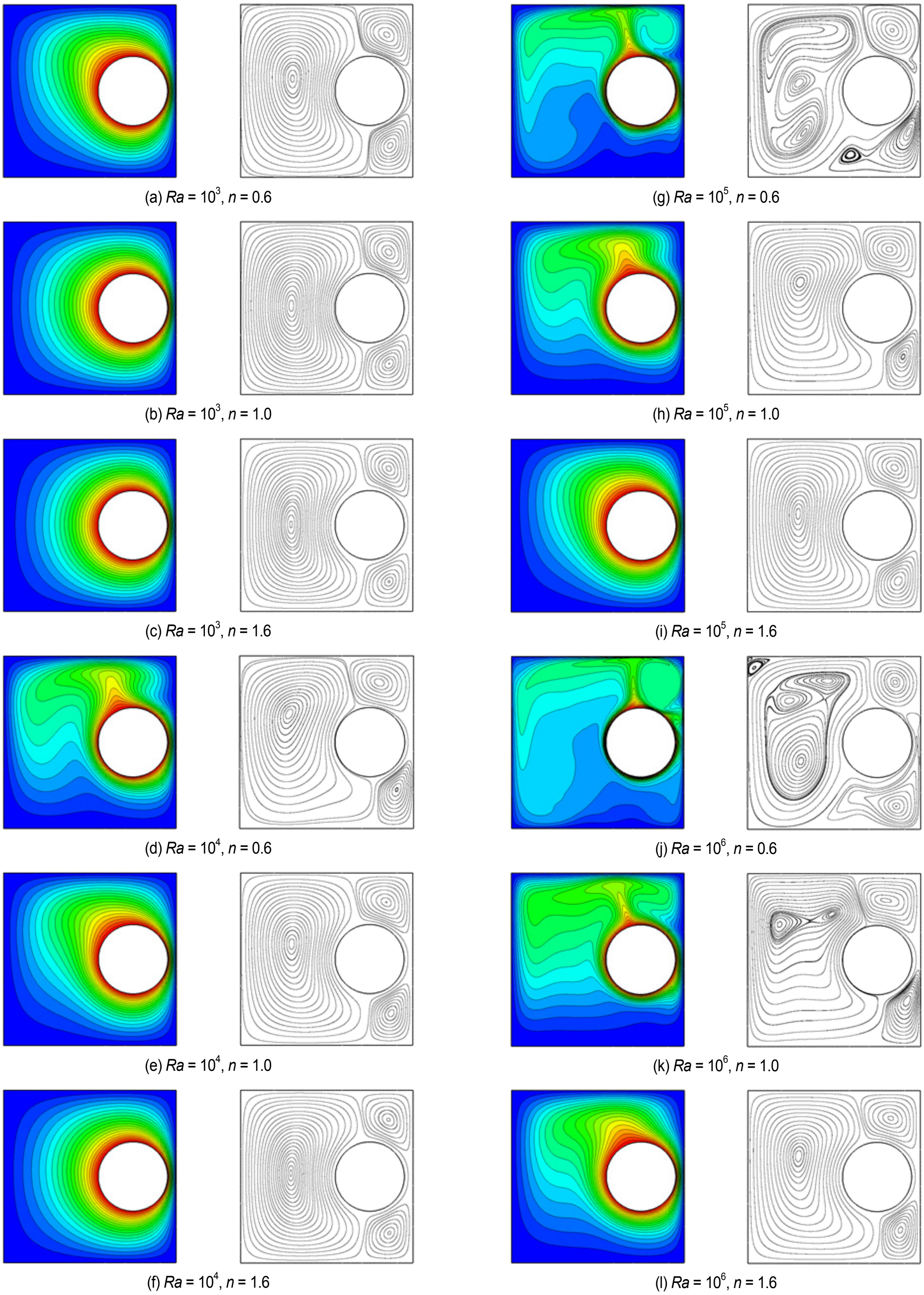

Fig. 6. Time-averaged isotherms and streamlines at $Pr = 10$ and $n = 0.6$, 1.0 and 1.6 for $\delta = 0.25L$ for various Ra.

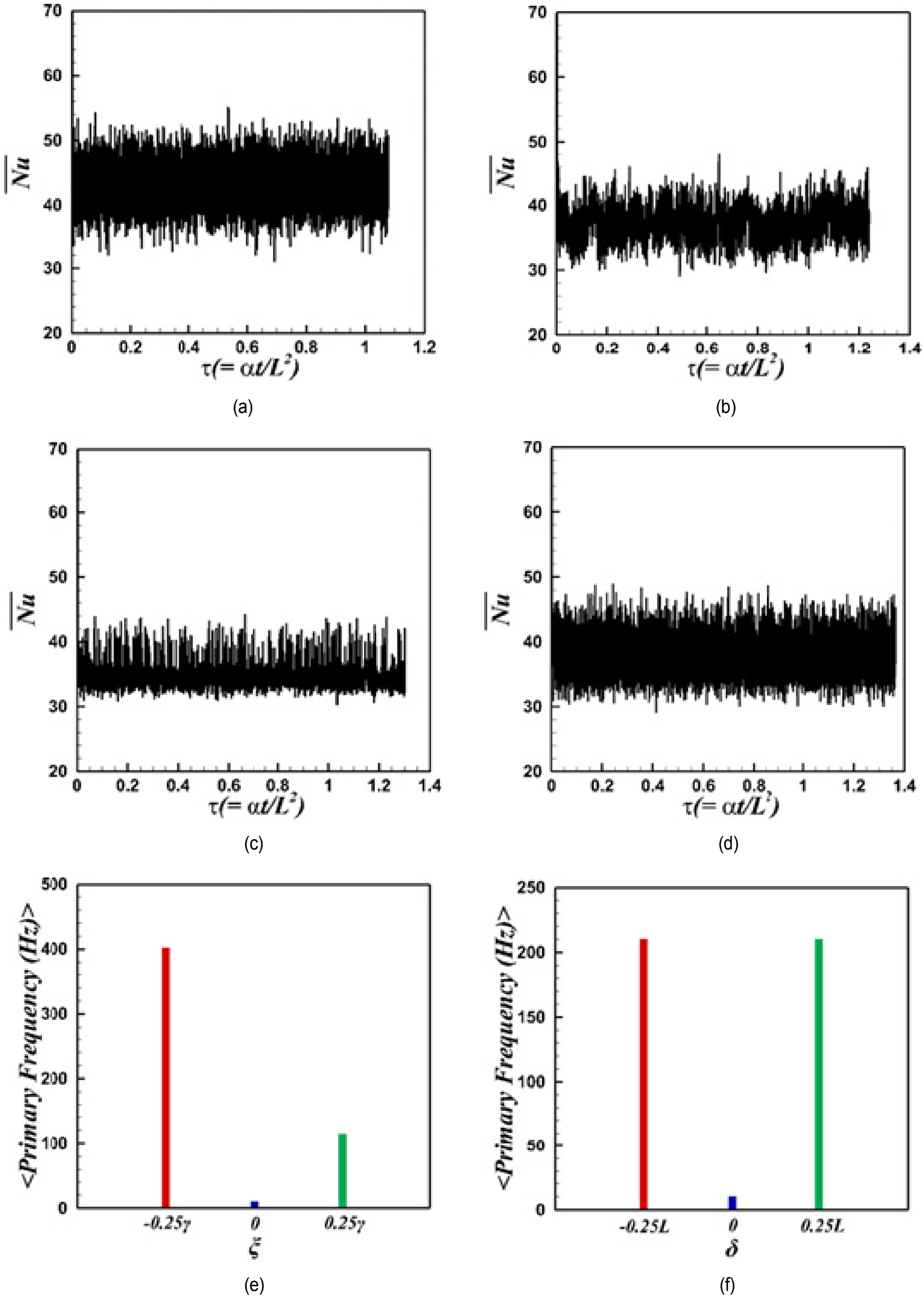

Fig. 7. Evolution of $\overline{Nu}$ for (a) ξ = -0.25γ; (b) ξ = 0; (c) ξ = 0.25γ; (d) δ = 0.25L at n = 0.6, Ra = 10^6. And Primary frequency distributions for (e) diagonal; (f) horizontal movements of inner cylinder.

local peaks appear in the distributions of $\langle Nu \rangle$ at φ = 90° and 180° for n = 0.8-1.6. However, due to increasing shear thinning effects, $\langle Nu \rangle$ at n = 0.6 shows a local peak at φ = 260° due to intensified thermal fields at φ = 260°, as shown in Fig. 4(g).

In common with Ra = 10^5, $\langle Nu \rangle$ at Ra = 10^6 shows a similar increasing trend in the range of 0° ≤ φ < 90°, followed by two peaks at φ = 90° and 180° and then a decreasing trend in the region to 180° < φ ≤ 340°. Finally, a small increase occurs until 360° or 0°. However, due to a thermal plume arising on the top right of the cylinder, $\langle Nu \rangle$ values increase much more than in

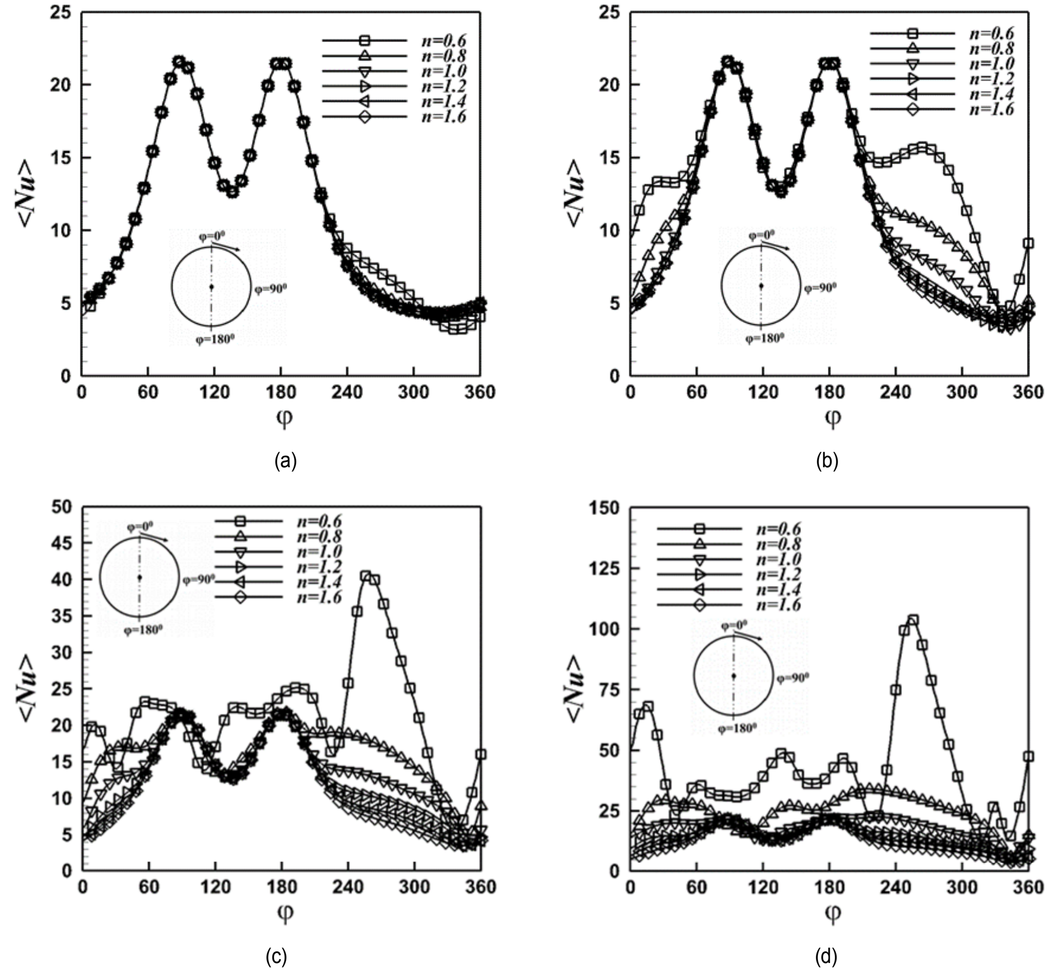

Fig. 8. $\langle Nu \rangle$ variation for (a) *Ra* = 10^3; (b) *Ra* = 10^4; (c) *Ra* = 10^5; (d) *Ra* = 10^6 and *ξ* = -0.25*γ*.

the case of *Ra* = 10^5 as *φ* increases from 0 to 10°, as shown in Fig. 8(d). The local peaks of $\langle Nu \rangle$ attain a maximum value at *φ* = 260°, and $\langle Nu \rangle$ is higher than that in the case of *Ra* = 10^5 due to increasing shear thinning effects at *n* = 0.6 and increased buoyancy convective flow.

The variations of $\langle Nu \rangle$ at *n* = 0.6 to 1.6 in the case of *ξ* = 0 are shown in Fig. 9. The distribution of $\langle Nu \rangle$ is shown only for half domain (0° ≤ *φ* < 180°) around the inner cylinder due to symmetry observed in the flow and thermal fields for all cases of *ξ* = 0, as reported by Pandey et al. [29]. In the case of *ξ = 0*, the distribution of $\langle Nu \rangle$ is almost symmetric about 90° (horizontal center line) at *Ra* = 10^3, as shown in Fig. 9(a). However, $\langle Nu \rangle$ shows an increasing pattern for *n* = 0.6 and 0.8 due to the small thermal plume rising above the cylinder towards the top wall at *Ra* = 10^4, as shown in Fig. 9(b). These small plumes makes the thermal boundary layer weaker on top of the cylinder surface at *Ra* = 10^4 and *ξ = 0*. The symmetry in the distribution of $\langle Nu \rangle$ about horizontal center line in the case of *ξ* = 0 disappears as the Rayleigh number increases to 10^5 and 10^6 at all power law indices. This results from the thermal plume appearing with increasing *Ra* and decreasing *n*, as shown in Figs. 9(c) and (d). The distribution of $\langle Nu \rangle$ at n = 0.6 and *Ra* = 10^5 shows a complex pattern of decreasing and increasing trends due to two upwelling and one down welling thermal plumes arising on top of inner circular cylinder, as reported by Pandey et al. [29]. In addition there appears two secondary vortices in flow fields. Moreover, the increment in $\langle Nu \rangle$ increases with decreasing power law index due to thinner thermal boundary layer developing across the inner cylinder for 0° ≤ *φ* < 180° and *Ra* = 10^6, as reported by Pandey et al. [29] and illustrated in Fig. 9(d).

The variations of $\langle Nu \rangle$ at *n* = 0.6 to 1.6 in the case of *ξ* = 0.25*γ* are shown in Fig. 10. The distribution of $\langle Nu \rangle$ at *Ra* = 10^3 shows two peak values at *φ* = 0°/360° and 270° irrespective of the *n*, as shown in Fig. 10(a). This is due to the much denser isotherms around the cylinder at *φ* = 0°/360° and 270°, as shown in Figs. 5(a)-(c). However, the distribution of $\langle Nu \rangle$ at *n* = 0.6 in the range of 120° ≤ *φ* ≤ 200° is somewhat different from other cases due to rising forward isotherms appearing around the surface of the cylinder. The distribution of $\langle Nu \rangle$ at *Ra* = 10^4 is similar to that at *Ra* = 10^3, especially at higher *n*, as shown in Fig. 10(b). However, with decreasing *n*, the local

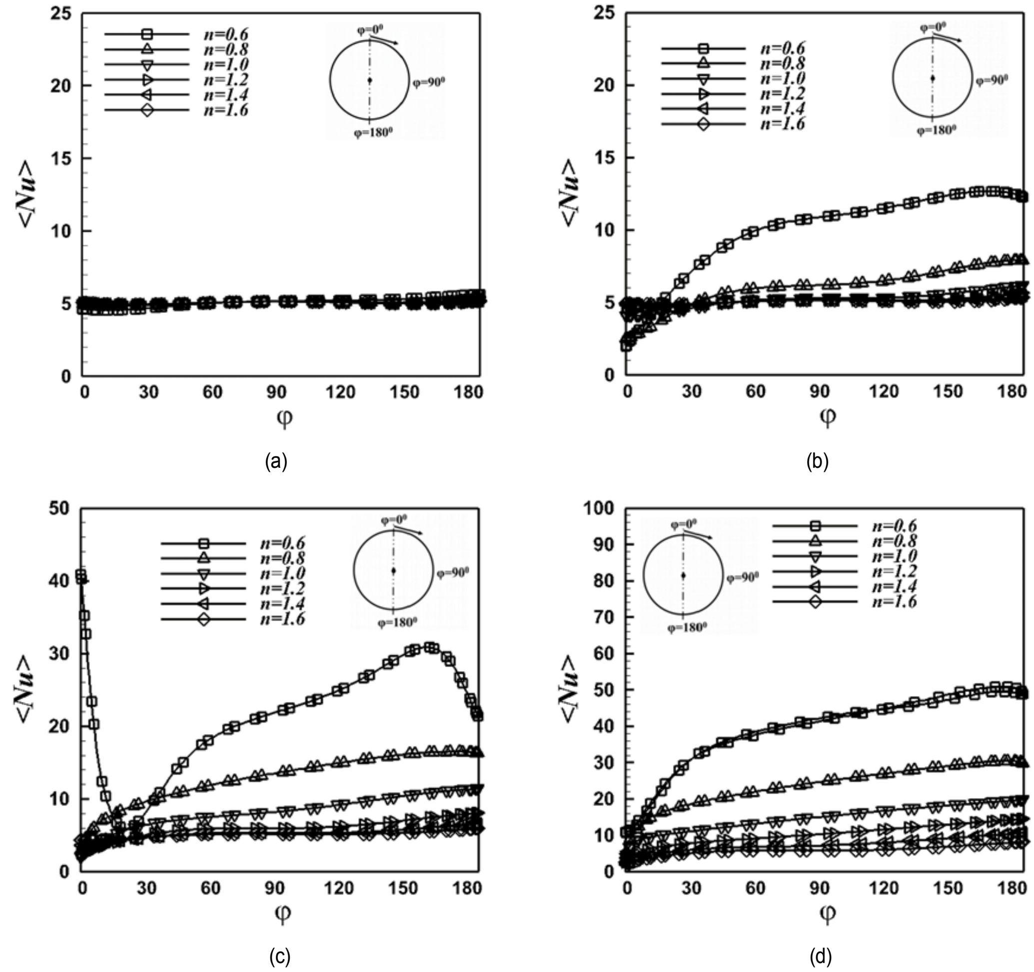

Fig. 9. $\langle Nu \rangle$ variation for (a) Ra = 10^3; (b) Ra = 10^4; (c) Ra = 10^5; (d) Ra = 10^6 and ξ = 0.

Nusselt number shows a somewhat different increasing trend with respect to φ except in the range of $70^o \le \varphi \le 220^o$. This is due to the slightly higher buoyancy-induced flow than at Ra = 10^3, as shown in Fig. 10(b). This increase in $\langle Nu \rangle$ values increases with decreasing power law index.

The distribution of $\langle Nu \rangle$ at Ra = 10^5 is similar to that at Ra = 10^4 except at n = 0.6, as shown in Fig. 10(c). The increasing $\langle Nu \rangle$ trend with decreasing n spans over a higher range of $60^o \le \varphi \le 240^o$, but at Ra = 10^4, the range was $70^o \le \varphi \le 220^o$. In addition, the peak value shifted to 310^o from 270^o due to rising plumes above the cylinder, as shown in Fig. 5(g). Two local peaks appear in the distributions of $\langle Nu \rangle$ at φ = $0^o/360^o$ and 270^o for n = 0.8-1.6.

Due to the thermal plume arising on the top right of the cylinder with increased buoyancy-induced flow, the increase in $\langle Nu \rangle$ in the case of n = 0.8-1.6 and Ra = 10^6 is much higher than in the case of Ra = 10^5 as φ increases from 60^o to 240^o, as shown in Fig. 10(d). Distorted thermal fields in between the cylinder and the left corner of the enclosure result in the distribution of $\langle Nu \rangle$ in the case of n = 0.6 that is somewhat different from other cases of n in the range of $0^o \le \varphi \le 50^o$. $\langle Nu \rangle$ Corresponding to a local peak at φ = 310^o was higher than at Ra = 10^5 due to increasing shear thinning effects at n = 0.6 and increased buoyancy convective flow.

For the case of δ = 0.25L, Fig. 11 shows the variations of $\langle Nu \rangle$ at n = 0.6 to 1.6. The distribution of $\langle Nu \rangle$ at Ra = 10^3 shows one peak value at φ = 90^o irrespective of n, as shown in Fig. 11(a). This is a result of denser thermal fields around the cylinder at φ = 90^o, as shown in Figs. 6(a)-(c). $\langle Nu \rangle$ at n = 0.6 is somewhat different from other cases in the range of $180^o \le \varphi \le 360^o$ due to slanted isotherms developing around the cylinder. The distribution of $\langle Nu \rangle$ at Ra = 10^4 is similar to that at Ra = 10^3, especially at higher n, as shown in Fig. 11(b). However, with decreasing n, $\langle Nu \rangle$ shows a somewhat different increasing and decreasing trends with respect to φ except in the range of $70^o \le \varphi \le 140^o$. This is due to the slightly higher buoyancy induced flow than at Ra = 10^3, as shown in Fig. 11(b).

The distribution of $\langle Nu \rangle$ at Ra = 10^5 is similar to that at Ra = 10^4 except at n = 0.6, as shown in Fig. 11(c). Due to increasing shear thinning effects, $\langle Nu \rangle$ at n = 0.6 shows two local peaks at φ = 30^o and 240^o. At Ra = 10^6, a thermal plume arises on the top right of the cylinder with increased buoyancy-induced flow.

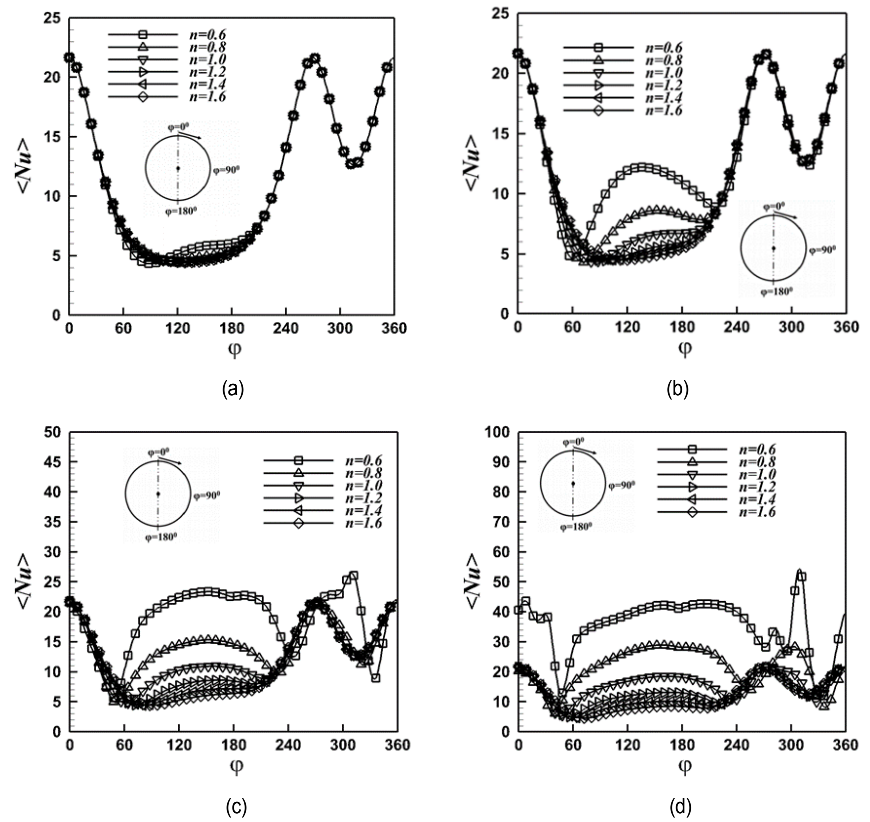

Fig. 10. $\langle Nu \rangle$ variation for (a) *Ra* = 10^3; (b) *Ra* = 10^4; (c) *Ra* = 10^5; (d) *Ra* = 10^6 and $\xi = 0.25\gamma$.

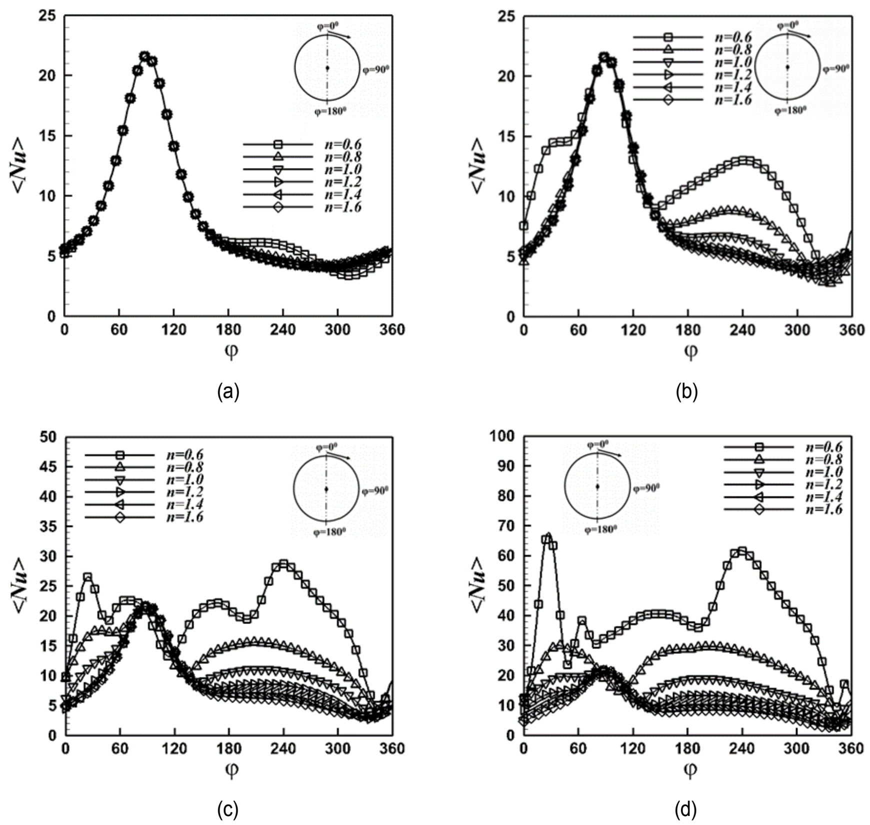

Fig. 11. $\langle Nu \rangle$ variation for (a) *Ra* = 10^3; (b) *Ra* = 10^4; (c) *Ra* = 10^5; (d) *Ra* = 10^6 and δ = 0.25L.

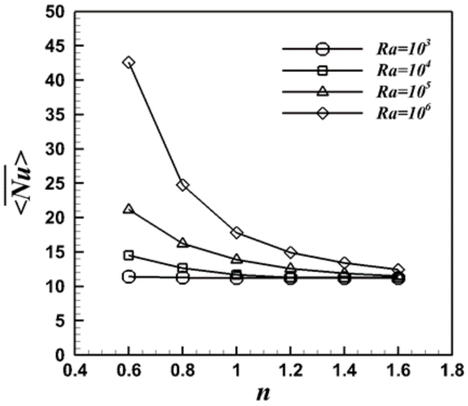

(a)

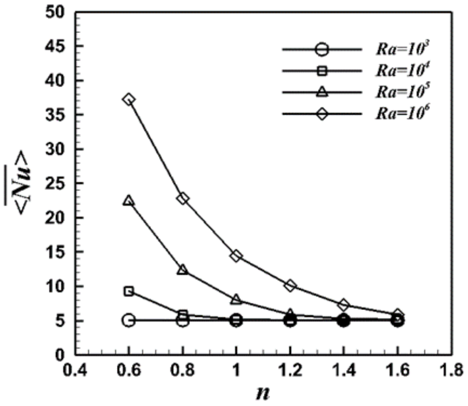

(b)

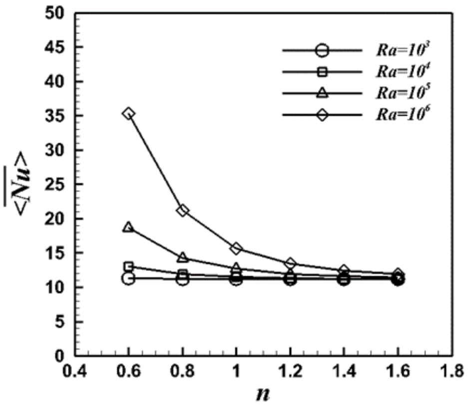

(c)

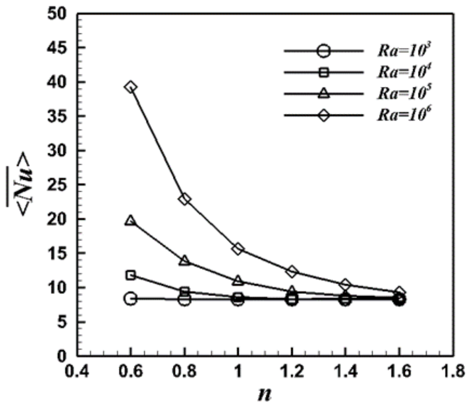

(d)

Fig. 12. $\langle \overline{Nu} \rangle$ in terms of n at various Ra for (a) ξ = -0.25γ; (b) ξ = 0; (c) ξ = 0.25γ; (d) δ = 0.25L.

As a result, the increase in $\langle Nu \rangle$ in the case of n = 0.8-1.6 is much higher than in the case of Ra = 10^5 as φ increases from 120^o to 340^o, as shown in Fig. 11(d). $\langle Nu \rangle$ corresponding to a local peak at φ = 30^o is higher than at Ra = 10^5 due to increasing shear thinning effects at n = 0.6 and increased buoyancy convective flow.

3.4 Distribution of surface-averaged Nusselt number

Figs. 12(a)-(d) show the distributions of $\langle \overline{Nu} \rangle$ versus n for various Ra with respect to cylinder location along the diagonal and horizontal center lines. $\langle \overline{Nu} \rangle$ is a decreasing function of n irrespective of the cylinder location. The maximum and minimum Nusselt numbers were found at ξ = -0.25γ and ξ = 0, respectively. The highest surface-averaged Nusselt number of 42.58 was found at n = 0.6 and Ra = 10^6 for ξ = -0.25γ, whereas the lowest value of 5.05 was found at n = 1.6 and Ra = 10^3 for ξ = 0.

$\langle \overline{Nu} \rangle$ always increases with increasing Ra for any given power index. However, this increase is more pronounced with decreasing n. $\langle \overline{Nu} \rangle$ decreases less with increasing n. The time and surface-averaged Nusselt number at n = 0.6 increases by 138.8 % with respect to n = 1 (Newtonian case) at Ra = 10^6 and ξ = -0.25γ. However, this increase for the cases of ξ = 0, ξ = 0.25γ, and δ = 0.25L was 158.7, 126.21 and 151.6 %, respectively. $\langle \overline{Nu} \rangle$ at n = 1.6 decreases by 30 % with respect to n = 1 (Newtonian case) at Ra = 10^6 and ξ = -0.25γ. However, this decrease for the cases of ξ = 0, ξ = 0.25γ, and δ = 0.25L was 59.45, 23.74, and 40.28 %, respectively.

Several correlations have been derived to estimate $\langle \overline{Nu} \rangle$ for given input parameters (Ra and n) at different positions of the cylinder:

Near the bottom right corner (ξ = -0.25γ):

$$\langle \overline{Nu} \rangle = \left[4.63 + 0.1 Ra^{0.42} \left(1 + 6.9 n^{2.3}\right)^{-1.4} \right]^{1.56} ; \; R^2 = 0.998$$

Near the top left corner (ξ = 0.25γ):

$$\langle \overline{Nu} \rangle = \left[29.72 + 0.34 Ra^{0.58} \left(1 + 15.54 n^{2.87}\right)^{-1.45} \right]^{0.71} ; \; R^2 = 0.999$$

Near the right wall (δ = 0.25L):

$$\langle \overline{Nu} \rangle = \left[38.57 + 4.8 Ra^{0.6} \left(1 + 7.4 n^{1.8}\right)^{-2.5} \right]^{0.57} ; \; R^2 = 0.998$$

4. Conclusions

The present research examined the effects of diagonal and horizontal movements of a cylinder on laminar natural convection. Based on the unsteady two-dimensional CFD analysis, it was found that the location of the cylinder affects temperature and velocity fields inside the cavity. The symmetry when the cylinder positioned at $\xi = 0$ no longer occurs when the cylinder moves across the horizontal centerline and diagonal of the enclosure. Flow bifurcation takes place at $n = 0.6$ (shear thinning fluid) at $Ra = 10^6$ irrespective of the cylinder location along the horizontal centerline and diagonal.

The maximum heat transfer rate around the cylinder occurred when the cylinder was placed near the bottom right corner ($\xi = -0.25\gamma$). However, when the cylinder was near the top left corner ($\xi = 0.25\gamma$), the heat transfer rate decreased in comparison to when the cylinder was near the bottom right corner ($\xi = -0.25\gamma$). The maximum increase was 158.7 % in $\langle \overline{Nu} \rangle$ at $n = 0.6$, $Ra = 10^6$ and $\xi = 0$ compared to the Newtonian fluid case ($n = 1$). The minimum decrease was 23.74 % at $n = 0.6$, $Ra = 10^6$ and $\xi = 0.25\gamma$ compared to the Newtonian fluid case ($n = 1$).

$\langle \overline{Nu} \rangle$ was a decreasing function of the power law index. The flow characteristics in the shear thinning regime were different from those in the shear thickening regime. In the case of heat enhancement applications, placing the cylinder near the bottom right corner shows the highest heat transfer rate. However, when less heat is desired, the cylinder must be placed at the center of the enclosure.

The time-averaged thermal and flow fields were found to be asymmetric when the cylinder is placed at a location other than at the center unlike the most of the cases of centrally placed cylinder ($\xi = 0$). The heat transfer characteristics within the enclosure enhance when the inner cylinder is placed close to the bottom wall ($\xi = -0.25\gamma$) in the shear thinning regime with increasing Rayleigh number. On the other hand, the heat transfer characteristics diminish when the inner cylinder is placed at the center ($\xi = 0$) in the shear thickening regime with decreasing Rayleigh number. The oscillatory motion of the thermal plume arising on top of inner cylinder was rapid as well as strong unlike the case of $\xi = 0$ resulting in highest dominant primary frequency of 402 Hz. On the other hand, the lowest primary frequency of 10 Hz was recorded in the case of centrally placed cylinder ($\xi = 0$) due to the symmetrical isotherms and streamlines.

Acknowledgments

This work was supported by the National Research Foundation of Korea (NRF) grant funded by the Korea government (MSIT) (No. 2019R1A5A808320111).

Nomenclature

D	: Diameter of internal circular cylinder, m
G	: Grid
g	: Gravitational acceleration, m/s^2
H	: Apparent viscosity
k	: Thermal conductivity, W/mK
L	: Length of the enclosure, m
m	: Consistency index, Ns^2/m^2
N	: Total number of grid elements
N_c	: Number of circumferential grid points along the cylinder
Nu	: Instantaneous local Nusselt number
$\overline{Nu}$	: Instantaneous surface-averaged Nusselt number
$\langle Nu \rangle$	: Time-averaged local Nusselt number
$\langle \overline{Nu} \rangle$	: Time and surface-averaged Nusselt number
n	: Power law index
p	: Pressure, Pa
P	: Dimensionless pressure, $P = \dfrac{L^2 p}{\rho \alpha^2}$
Pr	: Prandtl number
Ra	: Rayleigh number
R	: Radius of internal circular cylinder, m
R^2	: Coefficient of multiple determination
T	: Temperature, K
T_0	: Reference temperature, K
T_m	: Mean temperature, K
ΔT	: Temperature difference between the hot and cold surfaces (T_h-T_c), K
t	: Time, s
u, v	: Velocities in x and y directions, m/s
U, V	: Dimensionless velocities in x and y directions,
x, y	: Cartesian coordinates in x and y directions, m
X, Y	: Dimensionless coordinates in x and y directions,
2D	: Two dimensional

Greek letters

α	: Thermal diffusivity, m^2/s
β	: Thermal expansion coefficient, 1/K
δ	: Distance of the center of circular cylinder from the center of the enclosure measured horizontally
η	: Effective viscosity, Ns/m^2
ρ	: Density, Kg/m^3
φ	: Angle of internal cylinder
θ	: Dimensionless temperature,
τ	: Dimensionless time, $\tau = \dfrac{t\alpha}{L^2}$
ξ	: Distance between the center of circular cylinder and center of enclosure measured diagonally

Superscripts and subscripts

c	: Cold/cooled
h	: Hot/heated
m	: Mean

References

[1] S. Ostrach, Natural convection in enclosures, *Advances in Heat Transfer*, 8 (1972) 161-227.

[2] G. De Vahl Davis, Natural convection of air in a square cavity: A bench mark numerical solution, *International Journal for Numerical Methods in Fluids,* 3 (1983) 249-264.

[3] A. K. De and A. Dalal, A numerical study of natural convection around a square, horizontal, heated cylinder placed in an enclosure, *International Journal of Heat and Mass Transfer*, 49 (2006) 4608-4623.

[4] B. S. Kim, D. S. Lee, M. Y. Ha and H. S. Yoon, A numerical study of natural convection in a square enclosure with a circular cylinder at different vertical locations, *International Journal of Heat and Mass Transfer,* 51 (2008) 1888-1906.

[5] S. H. Hussain and A. K. Hussein, Numerical investigation of natural convection phenomena in a uniformly heated circular cylinder immersed in square enclosure filled with air at different vertical locations, *International Communications in Heat and Mass Transfer,* 37 (2010) 1115-1126.

[6] H. S. Yoon, M. Y. Ha, B. S. Kim and D. H. Yu, Effect of the position of a circular cylinder in a square enclosure on natural convection at Rayleigh number of 10^7, *Physics of Fluids,* 21 (2009) 047101.

[7] J. M. Lee, M. Y. Ha and H. S. Yoon, Natural convection in a square enclosure with a circular cylinder at different horizontal and diagonal locations, *International Journal of Heat and Mass Transfe*r, 53 (2010) 5905-5919.

[8] D. H. Kang, M. Y. Ha, H. S. Yoon and C. Choi, Bifurcation to unsteady natural convection in square enclosure with a circular cylinder at Rayleigh number of 10^7, *International Journal of Heat and Mass Transfer,* 64 (2013) 926-944.

[9] H. S. Yoon, J. H. Jung and Y. G. Park, Natural convection in a square enclosure with two horizontal cylinders, *Numerical Heat Transfer, Part A: Applications,* 62 (2012) 701-721.

[10] Y. G. Park, M. Y. Ha, C. Choi and J. Park, Natural convection in a square enclosure with two inner circular cylinders positioned at different vertical locations, *International Journal of Heat and Mass Transfer,* 77 (2014) 501-518.

[11] Y. G. Park, H. S. Yoon and M. Y. Ha, Natural convection in square enclosure with hot and cold cylinders at different vertical locations, *International Journal of Heat and Mass Transfer,* 55 (2012) 7911-7925.

[12] Y. G. Park, M. Y. Ha and H. S. Yoon, Study on natural convection in a cold square enclosure with a pair of hot horizontal cylinders positioned at different vertical locations, *International Journal of Heat and Mass Transfer,* 65 (2013) 696-712.

[13] Y. G. Park, M. Y. Ha and J. Park, Natural convection in a square enclosure with four circular cylinders positioned at different rectangular locations, *International Journal of Heat and Mass Transfer,* 81 (2015) 490-511.

[14] Y. M. Seo, Y. G. Park, M. Kim, H. S. Yoon and M. Y. Ha, Two-dimensional flow instability induced by natural convection in a square enclosure with four inner cylinders. Part I: Effect of horizontal position of inner cylinders, *International Journal of Heat and Mass Transfer,* 113 (2017) 1306-1318.

[15] Y. M. Seo, G. S. Mun, Y. G. Park and M. Y. Ha, Two-dimensional flow instability induced by natural convection in a square enclosure with four inner cylinders. Part II: Effect of various positions of inner cylinders, *International Journal of Heat and Mass Transfer,* 113 (2017) 1319-1331.

[16] S. Pandey, Y. G. Park and M. Y. Ha, An exhaustive review of studies on natural convection in enclosures with and without internal bodies of various shapes, *International Journal of Heat and Mass Transfer,* 138 (2019) 762-795.

[17] A. Acrivos, A theoretical analysis of laminar natural convection heat transfer to non-Newtonian fluids, *AIChE Journal,* 6 (1960) 584-590.

[18] H. Ozoe and S. W. Churchill, Hydrodynamic stability and natural convection in Ostwald-de Waele and Ellis fluids: The development of a numerical solution, *AIChE Journal*, 18 (1972) 1196-1207.

[19] M. L. Ng and J. P. Hartnett, Natural convection in power law fluids, *International Communication in Heat and Mass Transfer,* 13 (1986) 115-120.

[20] M. Ohta, M. Akiyoshi and E. Obata, A numerical study on natural convective heat transfer of Pseudoplastic fluids in a square cavity, *Numerical Heat Transfer, Part A: Applications,* 41 (2002) 357-372.

[21] G. B. Kim, J. M. Hyun and H. S. Kwak, Transient buoyant convection of a power-law non-Newtonian fluid in an enclosure, *International Journal of Heat and Mass Transfer,* 46 (2003) 3605-3617.

[22] M. Lamsaadi, M. Naimi and M. Hasnaoui, Natural convection of non-Newtonian power law fluids in a shallow horizontal rectangular cavity uniformly heated from below, *Heat and Mass Transfer,* 41 (2005) 239-249.

[23] M. Lamsaadi, M. Naimi, M. Hasnaoui and M. Mamou, Natural convection in a vertical rectangular cavity filled with a non-Newtonian power law fluid and subjected to a horizontal temperature gradient, *Numerical Heat Transfer, Part A: Applications,* 49 (2006) 969-990.

[24] M. Lamsaadi, M. Naimi, M. Hasnaoui and M. Mamou, Natural convection heat transfer in shallow horizontal rectangular enclosures uniformly heated from the side and filled with non-Newtonian power law fluids, *Energy Conversion and Management*, 47 (2006) 2535-2551.

[25] O. Turan, A. Sachdeva, N. Chakraborty and R. J. Poole, Laminar natural convection of power-law fluids in a square enclosure with differentially heated side walls subjected to constant temperatures, *Journal of Non-Newtonian Fluid Mechanics*, 166 (2011) 1049-1063.

[26] O. Turan, A. Sachdeva, R. J. Poole and N. Chakraborty, Aspect ratio and boundary conditions effects on laminar natural convection of power-law fluids in a rectangular enclosure with differentially heated side walls, *International Journal of Heat and Mass Transfer*, 60 (2013) 722-738.

[27] O. Turan, J. Lai, R. J. Poole and N. Chakraborty, Laminar natural convection of power-law fluids in a square enclosure submitted from below to a uniform heat flux density, *Journal of*

Non-Newtonian Fluid Mechanics, 199 (2013) 80-95.

[28] M. H. Matin and W. A. Khan, Laminar natural convection of non-Newtonian power-law fluids between concentric circular cylinders, *International Communications in Heat and Mass Transfer*, 43 (2013) 112-121.

[29] S. Pandey, Y. G. Park and M. Y. Ha, Unsteady analysis of natural convection in a square enclosure filled with non-Newtonian fluid containing an internal cylinder, *Numerical Heat Transfer, Part B: Fundamentals*, 77 (2020) 1-21.

[30] S. V. Patankar, *Numerical Heat Transfer and Fluid Flow*, Hemisphere, Washington, DC (1980).

Sudhanshu Pandey received his M.S. degree from Indian Institute of Technology Madras, India in 2016, and pursuing Ph.D. at Pusan National University, Korea. His research interests are focused on natural convection, non-Newtonian fluids and computational fluid dynamics.

Yong Gap Park received his B.S. degree from Pusan National University, Korea, in 2008, and Ph.D. degree from Pusan National University, Korea in 2014. Dr. Park is currently a Professor at the School of Mechanical Engineering, Changwon National University in Changwon. His research interests are focused on natural convection, heat exchanger and computational fluid dynamics.

Man Yeong Ha received his B.S. degree from Pusan National University, Korea, in 1981, M.S. degree, in 1983, from Korea Advanced Institute of Science and Technology, Korea, and Ph.D. degree from Pennsylvania State University, USA in 1990. Dr. Ha is currently a Professor at the School of Mechanical Engineering at Pusan National University in Busan, Korea. He served as an Editor of the Journal of Mechanical Science and Technology. He is the member of Honorary Editorial Advisory Board of the International Journal of Heat and Mass Transfer. His research interests are focused on thermal management, computational fluid dynamics, and micro/nano fluidics.